

Propagating Rifts: The Roles of Crustal Damage and Ascending Mantle Fluids

Folarin Kolawole^{1,2}, Rasheed Ajala¹

¹Lamont-Doherty Earth Observatory of Columbia University, Palisades, New York, 10964, United States

²Department of Earth and Environmental Sciences, Columbia University, New York, 10027, United States

Correspondence to: Folarin Kolawole (fola@ldeo.columbia.edu)

Abstract

We investigate the upper-crustal structure of the Rukwa-Tanganyika Rift Zone, East Africa, where the Tanganyika Rift is interacting with the Rukwa and Mweru-Wantipa rift tips, manifested by prominent fault scarps and seismicity across the rift interaction zones. We invert earthquake P and S travel times to produce three-dimensional upper-crustal velocity models for the region and perform seismicity cluster analysis to understand strain accommodation at rift interaction zones and the propagating rift tips. The resulting models reveal the occurrence of anomalously high V_p/V_s ratios in the upper-crust beneath the Rukwa and Mweru-Wantipa rift tips — regions with basement exposures and sparse rift sedimentation. We detect distinct earthquake families within the deeper clusters which exhibit an upward linear temporal evolution pattern that suggests triggering by upward fluid migration and creep failure. A spatial transition from proximal tip zones dominated by thinned crust and through-going crustal and upper-mantle seismicity to distal tip zones with thick crust and dominantly upper-crustal seismicity indicate an along-axis variation in the controls on rift tip deformation. Overall, the collocation of basement faulting, crustal and upper mantle seismicity, and upper-crustal high V_p/V_s ratios suggest a mechanically weakened crust at the rift tips, likely accommodated by brittle damage from crustal bending strain and thermomechanical alteration by ascending fluids (mantle-sourced volatiles, and hydrothermal fluids). These findings provide new insights into the physics of continental rift tip propagation, linkage, and coalescence — a necessary ingredient for initiating a continental break-up axes.

1 Introduction

The mechanism of segmentation and lateral propagation and linkage of continental rifts, first introduced by Bosworth (1985), has received significant attention from the scientific community as they influence the structure and temporal progression of the evolving break-up axis (e.g., Ebinger et al., 1989, 1999; Nelson et al., 1992; Acocella, 1999; Aanyu and Koehn, 2011; Allken et al., 2012; Corti, 2004; Zwaan et al., 2016; Neuharth et al., 2021; Kolawole et al., 2021a; Brune et al., 2023). Previous studies have established that continental rift systems grow by initial nucleation of isolated segments that propagate laterally, interact, link up, and coalesce to form longer composite rift basins with a continuous rift floor. Prior to linkage, the propagating rift segments are separated by an ‘unrifted’ crustal block, and the lateral propagation of the rift deformation into the intervening block is essential to advance the rift system towards break-up (e.g., Nelson et al., 1992; Kolawole et al., 2021a; Brune et al., 2023).

32 In regions of active tectonic extension, inelastic deformation manifests by tectonic and magmatic deformation of the crystalline
33 crust and its overlying sedimentary sequences in the rift basins (e.g., Brune et al., 2023; Pérez-Gussinyé et al., 2023). However,
34 in magma-poor (i.e., non-volcanic) active rift settings, tectonic deformation in continental rifts is commonly accommodated
35 by widespread brittle deformation of the crust through faulting and fracturing and accompanied by earthquakes (e.g., Muirhead
36 et al., 2019; Kolawole et al., 2017, 2018; Gaherty et al., 2019; Zheng et al., 2020; Stevens et al., 2021). Nevertheless, little is
37 known of how this deformation is transferred onto the propagating rift tips, and long-standing questions remain on how the
38 earth's crystalline crust accommodates and localizes tectonic strain during continental rift propagation.

39 In this study, we use recently acquired seismic data to explore the upper crustal structure of the Rukwa-Tanganyika Rift Zone
40 (Fig. 1a), an active non-volcanic rift zone along the East African Rift System, where previous studies have suggested a thick,
41 strong lithosphere (Craig et al., 2011; Foster and Jackson, 1998; Yang and Chen, 2010; Hodgson et al., 2017; Lavayssière et
42 al., 2019) and ongoing unilateral propagation of the Rukwa Rift tip (Kolawole et al., 2021a). A previous study (Hodgson et
43 al., 2017) utilized the receiver function technique to map the spatial distribution of crustal-averaged V_p/V_s ratios but lacked
44 constraints on the shallowest structure. Our results provide insight into the fundamental mechanism of strain distribution and
45 localization along actively propagating rift segments. Ultimately, the approach may advance our understanding of how
46 incipient divergent plate boundaries mature within active continental environments.

47 **2 The Rukwa-Tanganyika Rift Zone**

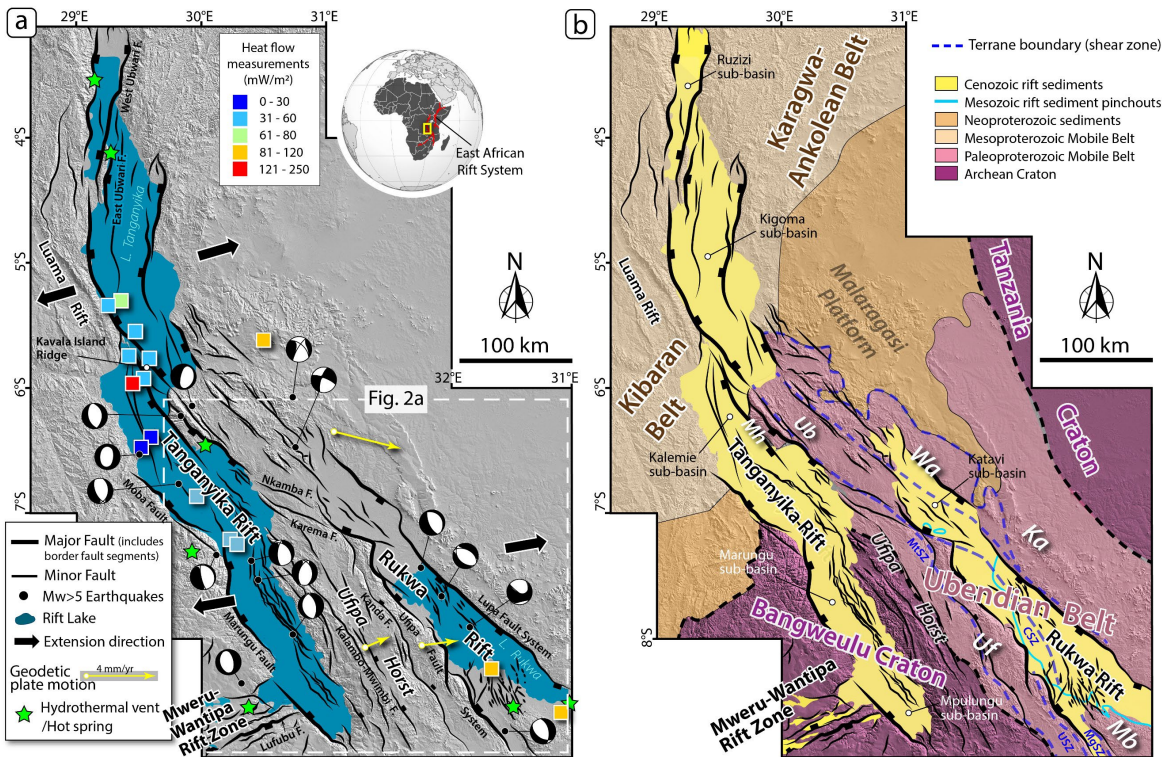
48 **2.1 Pre-Rift Crystalline Basement**

49 The crystalline crust of the Rukwa-Tanganyika Rift Zone (Fig. 1a) is mainly composed of metamorphic and igneous rocks of
50 the Paleoproterozoic (1.85–1.95 Ga) Ubendian mobile belt (Fig. 1b), flanked by Archean crystalline rocks of the Bangweulu
51 and Tanzania cratons and their overlying Neoproterozoic sedimentary sequences to the southwest and northeast respectively
52 (Fig. 1b). The Ubendian Belt consists of several amalgamated NW-trending terranes defining the orogenic belt that
53 accommodated the Paleoproterozoic collision events (2.025–2.1 Ga) between the Tanzania Craton and the Bangweulu Block.
54 The terranes, comprising Ufipa, Katuma, Wakole, Lupa, Mbozi, Ubende, and Upangwa (Fig. 1b; Daly, 1988; Lenoir et al.,
55 1994), are now exhumed due to long-term erosion and are bounded by steeply-dipping, ductile, amphibolite facies, strike-slip
56 shear zones (Fig. 1b; Daly, 1988; Lenoir et al., 1994; Theunissen et al., 1996; Kolawole et al., 2018, 2021b; Lemna et al.,
57 2019; Heilman et al., 2019; Ganbat et al., 2021). Their associated ductile fabrics are suggested to have influenced the
58 development of post-Precambrian rift basins in the region (Wheeler and Karson, 1994; Theunissen et al., 1996; Klerkx et al.,
59 1998; Boven et al., 1999; Heilman et al., 2019; Lemna et al., 2019; Kolawole et al., 2018, 2021a,b).

60

61 **2.2 Phanerozoic Rifting History**

62 The Rukwa-Tanganyika Rift Zone is defined by a system of NNW-to-NW-trending overlapping rift segments, consisting of
 63 the Tanganyika Rift, the Rukwa Rift to its southeast, and the ENE-trending Mweru-Wantipa Rift located just southwest of
 64 Tanganyika's southernmost sub-basin (Figs. 1a-b). The rift zone records multiple phases of Phanerozoic tectonic extension,
 65 with the first phase occurring in the Late Permian to Triassic, the second phase beginning in the Late Jurassic but peaking in
 66 the Cretaceous, and the third phase initiating in the Late Oligocene and presently persisting (e.g., Delvaux, 1989, Roberts et
 67 al., 2012). Although studies show that all the rift segments are currently active (e.g., Daly et al., 2020; Hodgson et al.,
 68 Lavayssiere et al., 2019; Heilman et al., 2019; Kolawole et al., 2021a), not all the basins record the three phases of Phanerozoic
 69 rifting (Delvaux, 1989; Morley et al., 1992, 1999; Muirhead et al., 2019; Shaban et al., 2023). Within the rift zone, the Rukwa
 70 Rift is the only basin with basement-penetrating borehole logs to constrain seismic reflection interpretation, producing detailed
 71 mapping of the lateral extents of the Mesozoic and Cenozoic syn-rift sequences (Morley et al., 1992) and relationships with
 72 rift faulting patterns (Morley et al., 1992, 1999; Heilman et al., 2019; Kolawole et al., 2021b). The distribution of the syn-rift
 73 deposits and faulting patterns show that the Rukwa Rift progressively elongated northwestwards and southeastwards over its
 74 polyphase extensional tectonic history (Morley et al., 1999; Heilman et al., 2019; Kolawole et al., 2021b).



75
76
77
78
79
80
81
82
83
84
85
86
87
88
89
90
91
92
93
94
95
96
97
98
99
100
101
102 **Figure 1. (a)** Tectonic map of the Rukwa-Tanganyika Rift Zone showing the rift faults (Morley et al., 1999; Muirhead et al., 2019; Kolawole
 103 et al., 2021a). Focal mechanisms and epicenters of Mw >5 earthquakes from National Earthquake Information Center (NEIC) catalog (1976–
 104 2018) obtained through the United States Geological Survey website (<https://earthquake.usgs.gov/earthquakes/search/>). Geodesic plate
 105 motion vectors are from Stamps et al. (2008). Regional extension directions are from Delvaux and Barth (2010) for the northern Tanganyika

106 Rift and Lavayssière et al. (2019) for the southern Tanganyika and Rukwa rift basins. Heat flow measurements and their locations are from
107 Jones (2020). Sites of hot springs/hydrothermal vents are from Tiercelin et al. (1993), Lavayssière et al. (2019), Jones (2020), and Mulaya
108 et al. (2022). (b) Geological map of the region, showing the cratons, mobile belts, terranes of the Ubendian Belt and shear zones, and
109 Cenozoic syn-rift sediments (modified after Daly, 1988; Hanson, 2003; Delvaux et al., 2012; Kolawole et al., 2021a,b; Ganbat et al., 2021).
110 Ubendian Belt Terranes: Ka - Katuma, Mb - Mbozi, Mh - Mahale, Ub - Ubende, Uf - Ufipa, Wa - Wakole. Exhumed Precambrian shear
111 zones (Delvaux et al., 2012; Heilman et al., 2019): CSZ, Chisi Shear Zone; MgSZ, Mughese Shear Zone; MtSZ: Mtose Shear Zone; USZ:
112 Ufipa Shear Zone.
113
114

115 The Cretaceous rifting event included reactivated faulting, tectonic subsidence, and sedimentation in the Rukwa Rift and
116 Luama Rift (e.g., Veatch, 1935; Delvaux, 1991; Roberts et al., 2012). Cenozoic rifting initiated the development of rift basins
117 as segments of the East African Rift System, featuring the reactivation of the Rukwa Rift and the development of the
118 Tanganyika and the Mweru-Wantipa rift segments (e.g., Morley et al., 1999; Delvaux et al., 2001; Chorowicz, 2005; Daly et
119 al., 2020). Crustal thickness across the rift zones range 31.6 – 42 km (Hodgson et al., 2017; Njinju et al., 2019) and lithosphere
120 thickness 130 – 170 km (Njinju et al., 2019). The contemporary regional minimum compressive stress orientation is 074° in
121 the northern Tanganyika Rift (Delvaux and Barth, 2010) and 080° in the southern Tanganyika and Rukwa rifts (Lavayssière
122 et al., 2019) (Fig. 1a). Although contemporary regional stress in the Mweru-Wantipa Rift is unknown, the Mweru Rift, which
123 is its southwestern continuation, is shown to have a regional minimum compressive stress orientation of 118° (Delavaux &
124 Barth, 2010).
125

126 **2.3 Rift Faulting and Seismicity Patterns**

127 The Tanganyika Rift basin is bounded by a system of large border faults that alternate polarity along-trend of the basin (Versfelt
128 and Rosendahl, 1989) and include the Marungu Fault, the Kavala Island Ridge Faults, the West and East Ubwari Faults, and
129 the Moba Fault (Fig. 1a), whereas the large graben of the Rukwa Rift basin is bounded by laterally continuous border fault
130 systems of the Lupa Fault to the northeast and Ufipa Fault to the southwest (Heilman et al., 2019). The Ufipa Horst represents
131 the intervening basement block between the southern Tanganyika Rift and the Rukwa Rift and is accommodating active
132 deformation as evidenced by the ca. 100-km long scarps of the Kanda and Kalambo-Mwimbi Faults (Fig. 1a; Delvaux et al.,
133 2012; Kolawole et al., 2021). Moreover, two prominent fault scarps extend WNW from the Rukwa Rift tip across a basement
134 region to the eastern margins of the central Tanganyika Rift (Nkamba and Karema Faults; Fig. 1a). To the southwest, the
135 deformation zone of the Mweru-Wantipa Rift hosts a ca. 50-km-wide parallel fault cluster that defines its southeastern margin
136 within which the Lufuba Fault appears to have the greatest escarpment height (Fig. 1a).

137 The entire Rukwa-Tanganyika Rift Zone records widespread seismicity (Figs. 2a, c–d) that extends beyond 42 km depth,
138 indicating that the seismogenic layer of the rift includes the uppermost mantle (Fig. 2c–e; Lavayssière et al., 2019). The events
139 define clusters with focal mechanism solutions that suggest steep, deep-rooting, large normal faults (Lavayssière et al., 2019),
140 and highlight localized active crustal deformation zones beneath Tanganyika Rift, Rukwa Rift, the Ufipa Horst, and the
141 Mweru-Wantipa Rift (Fig. 1a). Across the rift zone, the earthquakes commonly continue down into the lower crust; however,

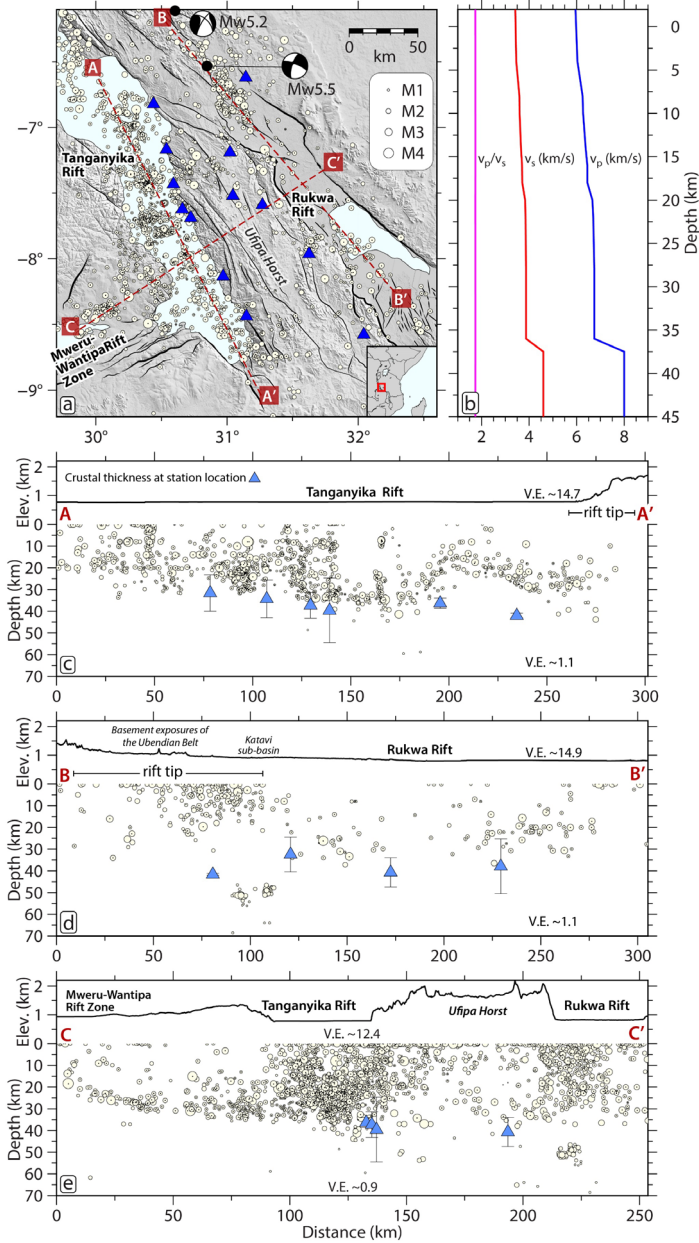
142 beneath the northwestern tip of the Rukwa Rift (Katavi sub-basin; Figs. 2a, 2d) the earthquakes occur in both the upper crust
143 and upper mantle (Lavyssière et al., 2019). More interestingly, the axis of the Rukwa Rift has sparse seismicity. Seismicity
144 clusters at the Rukwa Rift tip extend beyond the margins of the basin sediments, continuing outboard into the regions of the
145 exposed pre-rift basement (Figs. 2a and 2d). In the southern Tanganyika Rift, earthquakes mostly cluster within and along the
146 rift axis (Figs. 2a and 2c). Previous seismic receiver function and crustal anisotropy studies show evidence indicating the
147 presence of partial melt/volatiles in the lower crust (Hodgson et al., 2017; Ajala et al., 2024), and demonstrate how lower crustal
148 fluids promote strain localization (Ajala et al., 2024). Heat flow measurements in the rift zone show thermal anomalies in the
149 central Tanganyika Rift (<30 to 250 mW/m²), the south-central region of the Rukwa Rift (81 – 120 mW/m²), and within the
150 basement region ahead of the northwestern tip of the Rukwa Rift (81 – 120 mW/m²) (Fig. 1a; Jones, 2020). The thermal
151 anomaly north of the Rukwa Rift tip occurs near NW-trending fault splays and Mw>5 earthquake epicenters within the
152 basement region. Furthermore, hydrothermal vent and hot spring locations coincide with the border fault zones of the
153 Tanganyika Rift and the south-central part of the Rukwa Rift (Fig. 1a; Tiercelin et al., 1993; Lavyssière et al., 2019; Jones,
154 2020).

155 **2.4 Active Deformation Across the Rift Interaction Zones**

156 At a regional scale, the Rukwa and Tanganyika rift basins are separated by an elevated region of pre-rift basement with
157 widespread exposures of Precambrian metamorphic rocks (Figs. 1a-b; Kolawole et al., 2021a). This elevated region of rift
158 overlap includes the Ufipa Horst to its south, and the region between the northern tip of the Rukwa and the eastern flank of the
159 central Tanganyika Rift to its north. In a geodynamic context, the geometry of the overlap region defines an overlapping
160 parallel-to-oblique ‘rift interaction zone’ (Kolawole et al., 2021a) and is characterized by historical seismicity and active faults
161 that deform the modern surface (Delvaux et al., 2001; Lavyssière et al., 2019; Kolawole et al., 2021a). The faults include the
162 WNW-trending Karema and Nkamba faults, which splay westwards from the Rukwa Rift tip (Fig. 1a; Fernandez-Alonso et
163 al., 2001; Kolawole et al., 2021a), and NW-trending faults that extend northwards towards the margin of the northern
164 Tanganyika Rift (Kolawole et al., 2021a). The longitudinal surface relief morphology of the southern Tanganyika Rift shows
165 a significantly steeper gradient than that of the Rukwa Rift tip (‘rift tip’ in Fig. 2c versus 2d). Overall, the current stage of
166 evolution of the rift interaction zone based on the relief profile, stream flow patterns, and drainage morphologies is inferred to
167 be partially breached (Kolawole et al., 2021a). To the southwest, the Mweru-Wantipa Rift extends eastward and appears to be
168 hard-linked with the border fault of the western flank of the southern tip of the Tanganyika Rift. The region between the two
169 rifts defines an overlapping orthogonal rift interaction zone, and the continuation of Lake Tanganyika into the Mweru-Wantipa
170 Basin and the apparent coalescence of the rift floors of the two basins suggest a breached rift interaction zone between them
171 (Kolawole et al., 2021a).

172

173
 174
 175
 176
 177
 178
 179
 180
 181
 182
 183
 184
 185
 186
 187
 188
 189
 190
 191
 192
 193



194 **Figure 2.** (a) Map of the southern Tanganyika and Rukwa rift zone showing the local seismicity (white circles; from TANGA14 array –
 195 network ZV, Lavayssière et al., 2019) scaled by magnitude. The red dots represent events used in the inversion. Blue triangles represent
 196 the locations of the TANGA14 broadband seismometers; Black lines are faults; the thicker black lines highlight border faults; Red dashed lines
 197 are locations of seismicity profiles in c-e. Inset map shows the relative location in East Africa. (b) Starting model used in the seismic
 198 tomographic inversion (from Lavayssière et al., 2019). (c - e) Elevation and depth profiles showing projected seismicity (from Lavayssière
 199 et al., 2019) and estimated Moho depths (from Hodgson et al., 2017) along and across the rifts. Cross-sectional profiles A-A' and B-B'
 200 only show earthquakes within 25 km on both sides of the cross-section traces, and all Moho depth plots are projected from stations within
 201 50 km of the profiles.

202

203 **3 Data and Methods**204 **3.1 Seismic Data**

205 We focus on waveform data recorded by the TANGA14 array, comprising 13 broadband seismographs deployed along the
 206 Ufipa Plateau for 15 months from June 2014 through September 2015 (Fig. 2a; Hodgson et al., 2017). Using the origin times
 207 from the local earthquake catalog developed by Lavayssière et al. (2019) comprising 2213 events (Fig. 2a), we download the
 208 associated waveforms using the facilities of the EarthScope Consortium. The waveforms were then filtered with a Butterworth
 209 filter to accentuate the earthquake signal in the frequency band used in Lavayssière et al. (2019): 2 – 15 Hz. Arrival times for
 210 both P and S waves were manually picked on filtered seismograms resulting in 3187 P times from 1277 earthquakes (resp.
 211 3121 S times from 1261 earthquakes). We only made the travel time picks when the phases were clear and impulsive. We do
 212 not record uncertainty in arrival times during picking, nor do we pick multiple times to estimate the data variance.

213 **3.2 Crustal Imaging**214 **3.2.1 Backprojection Tomography**

215 Using our manually picked P and S arrival times, we develop 3D P and S velocity models for the Tanganyika-Rukwa region
 216 via nonlinear back-projection travel time inversion (Hole, 1992; Hole et al., 2000). For the study area, we use the 1-D P and S
 217 velocity model developed by Lavayssière et al. (2019) as our initial velocity model. We parameterize the model space using a
 218 fixed 5 km grid spacing with dimensions of 425 km x 435 km x 50 km. The bottom right corner of the model is 29.1651° E
 219 and -9.6764° S and extends from 7 km above sea level to 43 km depth. Therefore, we use the actual station elevations without
 220 needing static corrections. The travel time predictions in the model are calculated using a finite-difference solution for the
 221 Eikonal equation (Vidale, 1990), which allows travel times to be computed for all grid points in the model. Ray paths are then
 222 simultaneously traced for any number of source-receiver pairs using the gradient of the travel time field. Due to the reciprocity
 223 in the travel time computation, we treat the receivers as sources, thus requiring only 13 forward computations in each iteration.
 224 Following the forward calculation, we iteratively update the models, k , at each grid point, j , as follows:

$$u_{k+1}^j = u_k^j + \delta u_k^j, \quad (1)$$

225 where the slowness perturbations, δu , are calculated using simple back-projection as the average of the neighborhood ray
 226 paths, i.e.,

$$\delta u_k^j = \frac{1}{N} \sum_{cells} \sum_{rays} \frac{\delta t_{ray}}{l_{ray}}, \quad (2)$$

227 with δt and l being the associated traveltime residual and raypath length for the associated ray. We further smooth the
228 perturbations once they are determined for all grid points in the model using a 3D moving average filter to control the spatial
229 resolution and stabilize the inversion. This procedure is like higher-order Tikhonov regularization in the least squares nonlinear
230 inversion. We gradually reduce the size of the smoothing dimension after every five iterations to increase the spatial resolution
231 of the model. The final smoothing size of our model from the 26th iteration is $5 \times 5 \times 3$ grid points. Finally, the Vp/Vs ratio is
232 obtained by dividing the P and S velocity models.

233 **3.2.2 Model Reliability Assessment**

234 To assess the model uncertainty, we employ a combination of ray coverage maps, classical checkerboard reconstruction tests,
235 a custom synthetic model reconstruction test (targeted resolution test, e.g., Saeidi et al., 2024), and real data inversion using
236 different starting models to determine areas of the model reliable enough for interpretation (Figs. 3 – 5 and S2 – S18). We
237 generate the checkerboard models by adding 3D sinusoid functions to the initial velocity model (Fig. 2b) using similar
238 magnitudes in the amplitudes of the real, inverted model (Fig. 3). The observed travel time dataset is computed in the
239 checkerboard model and then inverted using the unperturbed starting model. We do not add noise to the synthetic datasets. We
240 also test different sizes of the anomalies (Figs. S4 – S15). Based on the results from the artificial reconstructions, we define a
241 polygon (e.g, Figs. S16 and 3) in the model space where the model parameters are reasonably resolved. Also, we developed
242 and inverted a custom synthetic model (Figs. S16 and S17) based on the vital features we interpret in our final preferred model
243 (Fig. 3) at the edge of the polygon where ray coverage is sparse or lacking (Fig. S2).

244 The synthetic model comprises three high Vp/Vs ($\sim 4\%$ increase) anomalies generated by perturbing the P (1% increase) and
245 S (3% decrease) velocity model and extending from 2 km above zero to 13 km depth in the model space, with the following
246 horizontal dimensions: 80 by 60 km at the north, 80 by 60 km at the southeast, and 65 by 85 km at the southwest. The inversion
247 results show good recovery of the anomalies with some smearing outside our predefined polygon (Fig. S17). To further assess
248 the reliability of these features in the real model (Fig. 3), we perform two other inversions of the real data using two different
249 3D initial velocity models from Celli et al. (2020) and van Herwaarden et al. (2023). A comparison of the results of all three
250 starting models (Figs. S18 – S20) shows that the Vp/Vs anomalies are robust.

251 **3.3 Seismicity Cluster Analysis**

252 Visual inspection of the seismicity (Fig. 2) shows apparent spatial clusters. However, we must perform a spatiotemporal
253 seismicity clustering analysis to determine which earthquakes are also close in time (Fig. S21). Although a complete statistical
254 study of the earthquake catalog is beyond the scope of the current research, we perform a simple clustering analysis (Fig. S22)
255 to highlight potential earthquake groups that could indicate fluid activity at the rift tips. First, we attempt catalog declustering
256 to remove any aftershock sequences using the approach of Reasenberg (1985) as implemented in the CLUSTER2000 program.
257 However, no significant aftershock sequences were found, with most aftershock clusters totaling 17 containing only two events

258 (Ajala & Kolawole, 2023). This is despite the earthquake frequency distribution (Fig. S23e) showing a decreasing amount of
 259 seismicity through time that would seemingly indicate the presence of aftershock sequences. The lack of correlation between
 260 the data availability periods when the seismic stations were operational (Fig. S23a) and the seismicity frequency (Fig. S23e)
 261 shows that there was indeed increased seismic activity during the earlier deployment times, particularly in August 2014. An
 262 enhanced earthquake catalog with a lower magnitude of completeness may be required in the region for declustering.
 263 Therefore, we decided to use the entire catalog as is in the clustering analysis. We analyze the earthquake catalog for clusters
 264 using the algorithm of Zaliapin et al. (2008) and Zaliapin & Ben-Zion (2013), as implemented by Goebel et al. (2019). For
 265 each event j in the catalog, except for the earliest one, we find the parent event, which is an earlier event, defined using the
 266 smallest nearest-neighbor distance η_{ij} computed to all the other events i and defined as

$$\eta_{ij} = \begin{cases} t_{ij}r_{ij}^{d_f}10^{-bm_i}, & t_{ij} > 0 \\ \infty, & t_{ij} \leq 0 \end{cases} \quad (3)$$

267
 268 where t_{ij} is the time separation in years, r_{ij} is the Haversine distance between the earthquake pairs epicenters, d_f is the fractal
 269 dimension of the epicenters assumed to be 1.6 (Zaliapin et al., 2008), b is the Gutenberg-Richter b-value set to 1, and m_i is
 270 the magnitude of the potential parent event i . To separate the nearest-neighbor distances into space R_{ij} and time T_{ij}
 271 components, we use the following relations,

$$T_{ij} = t_{ij}10^{-qbm_i}, \quad (4)$$

$$R_{ij} = r_{ij}^{d_f}10^{-(1-q)m_i}, \quad (5)$$

272
 273 where we assume an interpolation factor q of 0.5.
 274

275
 276 Finally, to split the catalog into background and cluster events, we estimate a separation threshold η_0 using the average of
 277 estimates of the 1st percentile of nearest-neighbor distances computed from 100 randomized catalogs with a similar range of
 278 space-time-magnitude parameters but with a Poissonian distribution representative of background seismicity (Fig. S22). At
 279 the estimated η_0 , we see the probability distribution of the nearest-neighbor distances deviate from the Weibull probability
 280 distribution known to represent Poisson background seismicity (Fig. S22c; Zaliapin & Ben-Zion, 2013). Event pairs with
 281 nearest-neighbor distances less than η_0 that have similar parents are then recursively grouped to generate the clustered catalog
 282 (Figs. 4, S23b – d, and S24). For clusters at the Rukwa rift tip, we compute the normalized cross-correlation coefficients of
 283 the vertical component of the waveforms of events relative to the waveform of the parent event (Figs. 4g and h). We note that
 284 the lack of uncertainties in the earthquake catalog (Lavayssière et al., 2019) and relative earthquake locations may introduce
 285 spatiotemporal errors in the above analysis. In presenting our results, we use the time-magnitude plots as a guide to help
 286 distinguish between the mechanisms of the two swarms as either slow slip (creep) or fluid flow (Roland & McGuire, 2009).
 287

288 4 Results

289 4.1 Crustal Seismic Velocity Models of the Tanganyika-Rukwa Rift Zone

290 We present the velocity models as perturbations (Fig. 3) relative to the starting models used in the inversion (Fig. 2b). The 5
291 km model grid spacing makes our selection of the 3 km depth maps (Figs. 3e, 3i, 4e, 4i, 5a, 5e, 5i) representative of the average
292 uppermost crustal structure of the model in the region, as can be verified in the cross-sectional profiles of Figure 5. The overall
293 distribution of upper crustal velocities generally reflects the near-surface geology, which serves as a primary constraint for
294 assessing the quality of the models. Our results show that lower V_p and V_s are collocated with the sedimentary basins of the
295 southern Tanganyika and Rukwa rifts. Relatively lower velocities continue along a narrow ESE-trending zone from the
296 Tanganyika Rift to the northern end of the Rukwa Rift, following the Nkamba and Karema faults. The Ufipa Horst separating
297 the Tanganyika and Rukwa rifts also shows localized zones of lower V_p , collocated with areas of prominent surface faulting
298 (Fig. 3a). However, unlike the V_p distribution, the Ufipa Horst is better defined in the V_s model, demonstrated by the relatively
299 higher values and structural continuity (Figs. 3e and h). Within the eastern section of the Mweru-Wantipa Rift and further east
300 towards the southern Tanganyika Rift, we observe moderate V_p anomalies collocated with moderate-to-low V_s anomalies
301 (Figs. 3a – b, e – f). Overall, the rift flanks and zones of widespread exposure of the pre-rift basement exhibit relatively higher
302 V_p and V_s .

303 The V_p/V_s ratio map (Fig. 3i) and cross-sections (Figs. 3j – l) show zones of anomalously high values that are restricted to
304 upper-crustal depths, the most prominent of which are A1: an anomaly at the northwestern end of the Rukwa Rift, an area
305 dominated by basement exposures and distributed faulting, A2: a broad anomaly extending across the eastern end of the
306 Mweru-Wantipa Rift through the transfer zone into the Tanganyika Rift, and A3: an anomaly in the southeastern interior of
307 the Rukwa Rift, collocated with the Ufipa Fault and the intra-basement Chisi Shear Zone (Fig. 1b). These highest V_p/V_s
308 anomalies commonly continue downward to 10 km or deeper (Figs. 3k – l) but our investigation focuses on the upper crust.

309 **4.2 Spatiotemporal Clustering of Rift Tip Seismicity**

310 Our cluster analysis yielded 115 clusters, but we only retained clusters with a minimum of 5 events, resulting in a filtered
311 number of 18 clusters. The distribution of these clusters is shown as colored circles in map and cross-section views in Figures
312 4a–d and Figure S24 and as functions of latitude, longitude, and depth in Figures S23b – d. We identify clusters throughout
313 the crust and in the upper mantle, with most of the clusters occurring along the intra-rift faults within the Tanganyika Rift.
314 Some clusters are located at the tips of the Mweru-Wantipa and Rukwa rifts and on faults within the Ufipa Horst. Due to the
315 focus of the current study on investigating rift tip processes, we only discuss the detected seismicity clusters at the Rukwa Rift
316 tip, the three spatially clustered events occurring at 10 – 20 km depth at the Mweru-Wantipa Rift tip, and the absence of clean
317 waveform records for these events preclude further analysis on these clusters.

318 There are two main clusters at the Rukwa rift tip (Figs. 4a – d), both occurring in the upper mantle between 40 – 70 km depths.
319 The northern cluster comprises six events with local magnitudes between 0.67 and 1.35 that happened within a period of ~50
320 minutes on July 9, 2014 (Fig. 4e). In contrast, the southern cluster has 12 events with magnitudes between 1.2 and 2.8 that
321 occurred within a period of ~19 days in June 2015 (Fig. 4f). We note the high waveform similarity of the events as recorded
322 at nearby stations (Figs. 4g and h). In general, both clusters define a generally linear trend with the shallower events occurring

323 later, indicating a generally upward migration (Figs. 4c and d). Although the relative timing of the largest magnitude event in
324 a cluster is often used as a proxy for defining aftershock sequences, here in the southern cluster, the magnitudes of the events
325 are low and primarily similar. Furthermore, the seismicity distribution does not follow Omori's decay law since our clustering
326 analysis would otherwise have detected it (Ajala & Kolawole, 2023).

327

328 **5 Discussion**

329 **5.1 Crustal Softening in the Rukwa-Tanganyika Rift Zone**

330 Brittle deformation in the crystalline crust, including fault- and folding-related damage, commonly creates zones of decreased
331 bulk crustal density, manifested as zones of anomalously low Vs and high Vp/Vs ratio (Allam et al., 2014; Fang et al., 2019).
332 Similarly, regions where brittle damage hosts melts/volatiles, and/or upwelling hydrothermal fluids are associated with
333 relatively higher Vp/Vs values (e.g., Chatterjee et al., 1985; Nakajima et al., 2001; Hua et al., 2019). In active rift settings with
334 absent surface volcanism, understanding the spatial distribution of upper-crustal seismic velocities permits the identification
335 of mechanically weakened zones where tectonic strain may be preferentially localized. Delineating these near-surface
336 structures will help to better understand how the crust accommodates tectonic strain along actively propagating rift basins and
337 predict ground motion amplification during large earthquakes (e.g., Cormier and Spudich, 1984; Ajala and Persaud, 2021).

338 In the Rukwa-Tanganyika Rift Zone, two of the three areas of the highest upper-crustal Vp/Vs ratios (A1 and A2) occur at rift
339 tips where syn-rift sedimentary cover is thinnest, and basement exposures dominate the surface geology (Figs. 1b and 3i).
340 These anomalies occur at or near geothermal anomalies (hot springs and high heat flow sites in Figs. 1a, 3i) and are collocated
341 with earthquake clusters and distributed normal faults. The anomalous seismicity cluster at the tip indicates the focus of active
342 brittle deformation of the crystalline crust in a region that is lacking well-developed rift basins. At the Rukwa Rift tip and
343 further to the northwest, the faulting pattern is generally characterized by distributed fault scarps that continue outboard from
344 the border faults into the rift interaction zone (Fig. 1a). At the Mweru-Wantipa Rift tip, the rift faults appear to mainly cluster
345 near the southeastern rift margin. Thus, we interpret the occurrence of the high upper-crustal Vp/Vs anomalies at the modern
346 rift tips to represent a zone of mechanically weakened crystalline crust.

347

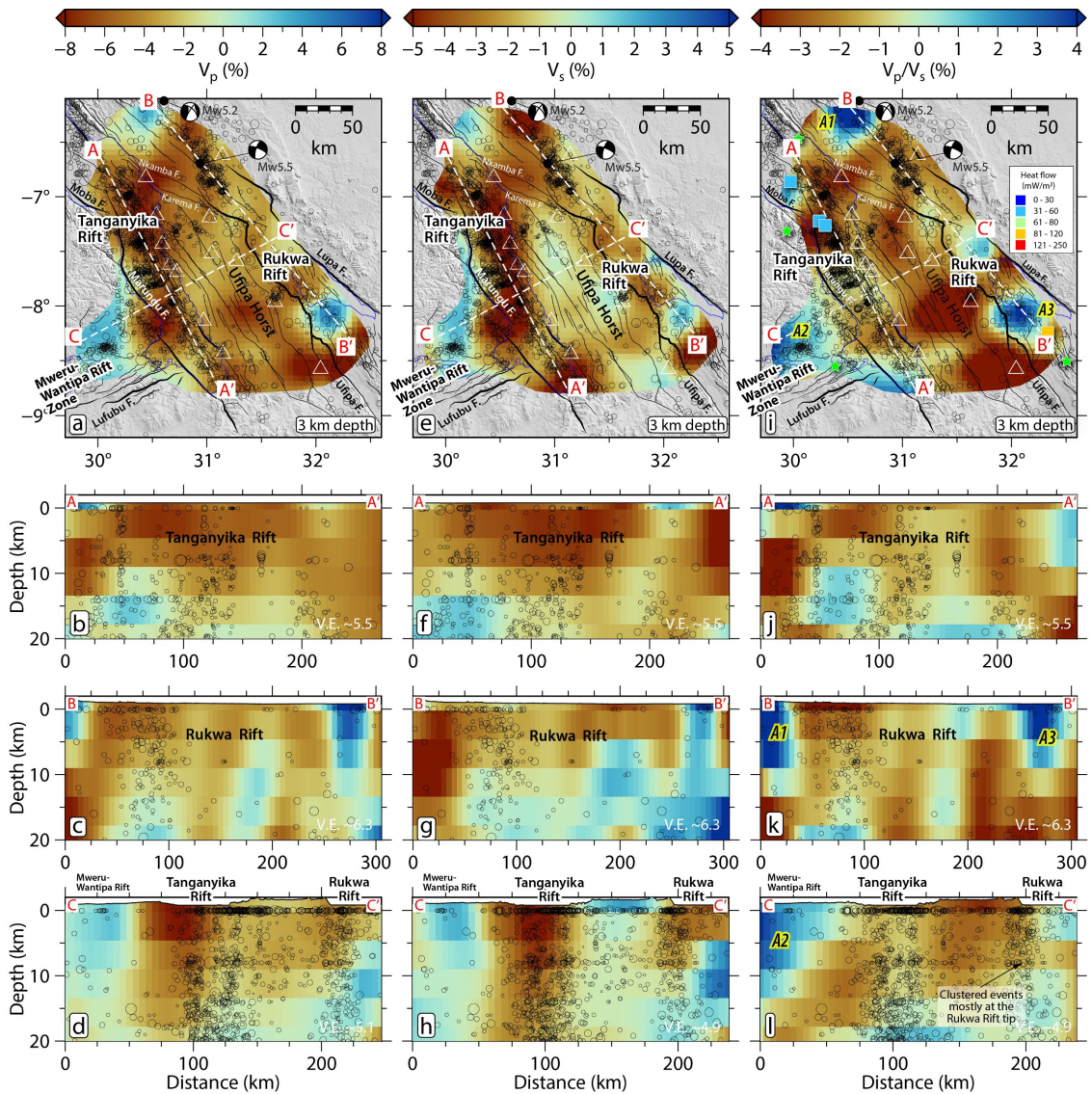


Figure 3. Maps and profiles through the tomographic models showing the perturbations relative to the starting models in Fig. 2b. (a) 3 km depth slice through the P wave velocity model. Unreliable areas of the model are not shown. Dashed black lines show the profile locations in b-d. (b – d) Profiles of the P wave velocity model. (e – h) Same as a-d but for the S wave velocity model. (i – l) Same as a-d but for the V_p/V_s ratios. Absolute values of the model parameters are shown in Fig. S16. Note that the geothermal center near anomaly A1 is north of latitude 6°S which is outside of the map coverage (see Fig. 1a).

375 **5.2 Mechanical Weakening of Rift Tips: The Roles of Bending Strain and Crustal Fluids**

376 The development of mechanically weakened crust at active rift tips reflects a critical rift process relevant for understanding
377 how continental rifts propagate. This is analogous to microfracture propagation driven by high-stress concentrations at the
378 crack tips (e.g., Kranz, 1979; Olson, 2004). Similarly, relatively large stress concentrations between interacting microcrack
379 tips (Kranz, 1979) agrees with interpretation of stress concentrations within rift interaction zones that separate propagating rift
380 tips (Kolawole et al., 2023). The northwestern tip of the Rukwa Rift is characterized by geomorphic features and tectonic
381 deformation patterns that suggest an ongoing northwestward propagation towards the central and northern Tanganyika Rift
382 (Kolawole et al., 2021a). The earthquake clusters at the Rukwa and Mweru-Wantipa rift tips (Fig. 2a) indicate that tectonic
383 stresses and elastic strain concentrations are focusing on the rift tip zones. The brittle deformation field that is manifested by
384 these earthquakes is likely accommodating the bending strain along the rift tip's flexural margin (Fig. 6a). Several studies have
385 demonstrated that crustal bending due to accumulated fault displacement, glacial unloading, thermal subsidence, or sediment
386 load induced crustal subsidence can focus significant strain in the upper crust, leading to brittle failure of the crust (e.g., Goetze
387 and Evans, 1979; Stein et al., 1979; Nunn, 1985). Here, long-term accrual of fault displacement and sediment loading along
388 the central hanging walls of the border faults causes basement down-flexure in the rift basin and proximal sections of the rift
389 tip, and contemporaneous basement upwarping at the distal section of the rift tip (Fig. 6a). The crustal bending at the rift tips
390 induces significant strain in the upper part of the brittle lithosphere, which may explain the prominent occurrence of
391 earthquakes at the rift tips, best expressed at the northwestern tip zones of the Rukwa Rift (Figs. 2a, 2d). Since there is no data
392 on the border fault displacements or basement depth variations from the rift axis into the areas of exposed basement ahead of
393 the rift tip, we cannot provide a detailed analysis of how the changes in basement flexure imposes extensional vs contractional
394 strain on the upper crust. Nevertheless, we suggest that damage clustering at a propagating rift tip is a relevant fundamental
395 process that may facilitate mechanical weakening at the tips of active continental rifts.

396 In addition to bending strain-related earthquakes in the crust, the temporal and upward linear trends of low-magnitude
397 seismicity migration in the upper mantle beneath the proximal rift tip in the Rukwa Rift tip (Figs. 4b-f) suggest fluid (volatiles)
398 related earthquake triggering. We interpret that the northern cluster likely represents fluid-induced microseismic creep due to
399 the fast migration velocity (>1 km/hr) (Fig. 4e), and the southern cluster likely indicates fluid flow due to the much slower
400 linear migration velocity (Fig. 4f) (e.g., Zhang & Shearer, 2016). These results are further corroborated by the high waveform
401 similarity of the events recorded at nearby stations (Figs. 4g and h; Raggiunti et al., 2023). In the Tanganyika Rift, the detected
402 spatiotemporally clustered events extend up from the moho to the upper-crust (Fig. S24), and the events are primarily in the
403 crust beneath the Mweru-Wantipa Rift tip (Fig. S24e). Although primarily hosted in the crust, we interpret that the detected
404 clustering events in the Tanganyika and Mweru-Wantipa are likely also triggered by fluids, and that the fluids are potentially
405 related to both mantle and hydrothermal sources. Thus, our cluster analysis results are consistent with previous studies that
406 suggest the presence of partial melt in the crust beneath Tanganyika Rift Zone (Hodgson et al., 2017; Lavaysseier et al., Ajala
407 et al., 2024).

408
409
410
411
412
413
414
415
416
417
418
419
420
421
422
423
424
425

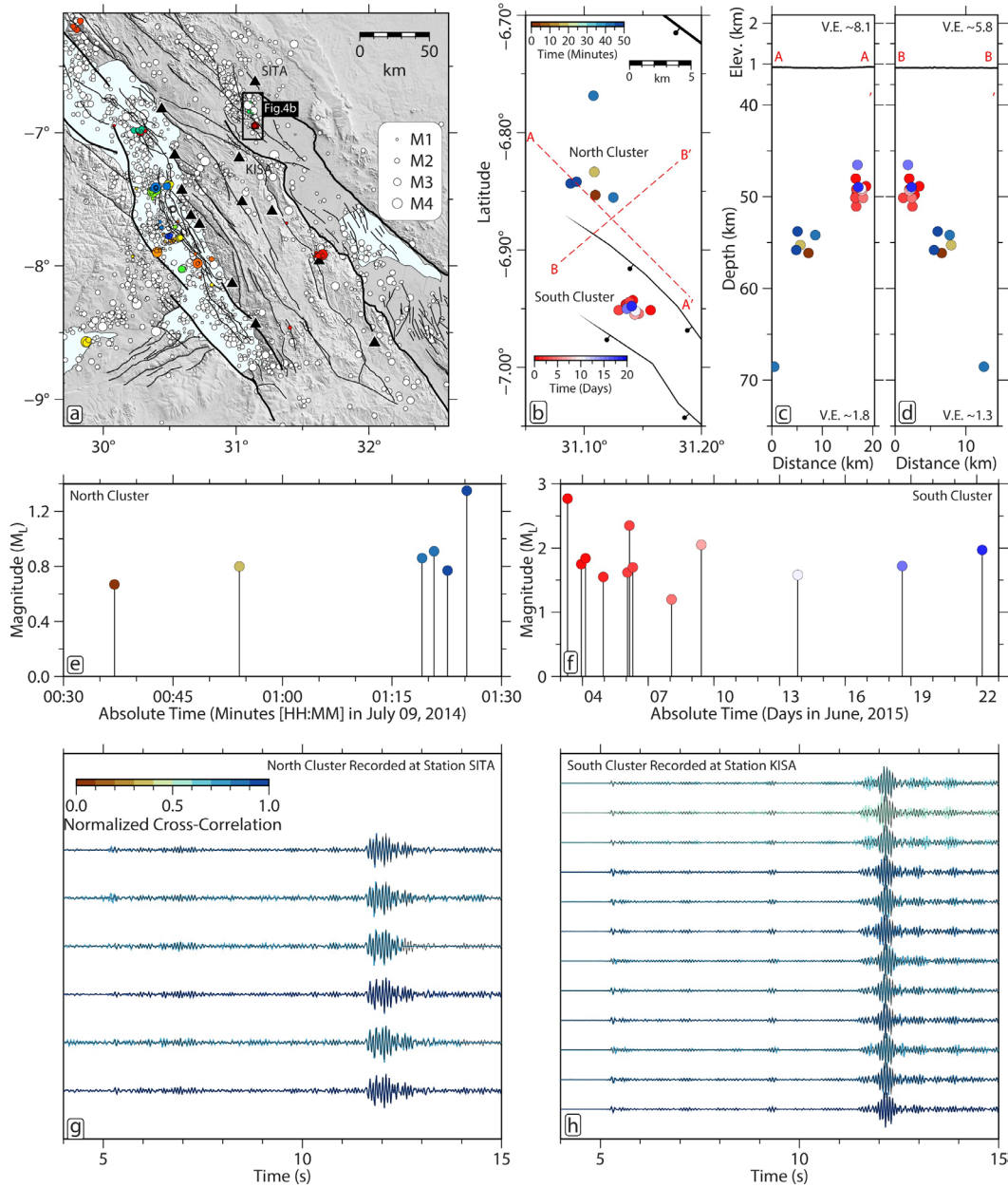


Figure 4. Delineation of spatiotemporal seismicity clusters with a focus on the Rukwa rift tip swarms. (a) Map of the study area showing the broad seismicity and detected spatiotemporal clusters (colored circles). Red polygon indicates the frame for the clusters shown in panel b. (b) Zoom-in map of the two clusters at the Rukwa tip color-coded according to their occurrence in time relative to the parent event (i.e., first event) in each group. Red dashed lines are the locations of the cross-sectional profiles in panels c and d. (c) Rift-parallel, and (d) Rift-perpendicular profiles showing the projected clusters. (e) Magnitude-time plot for the northern cluster events. (f) Magnitude-time plot for the southern cluster events. (g) 2–15 Hz waveform records for the north cluster events recorded at station SITA highlighted in panel a. Each waveform is colored using the normalized cross-correlation coefficient computed by comparing the similarity of each waveform in the sequence to the waveform of the parent event. The parent event waveform is also plotted on all the waveforms as a black line for visual comparison. All traces have been time-shifted to maximize the correlation. The maximum cross-correlation value occurs for the first trace

435 since it represents the autocorrelation (correlation of the parent waveform with itself). **(h)** Similar to panel g but for the southern cluster
436 recorded at station KISA.

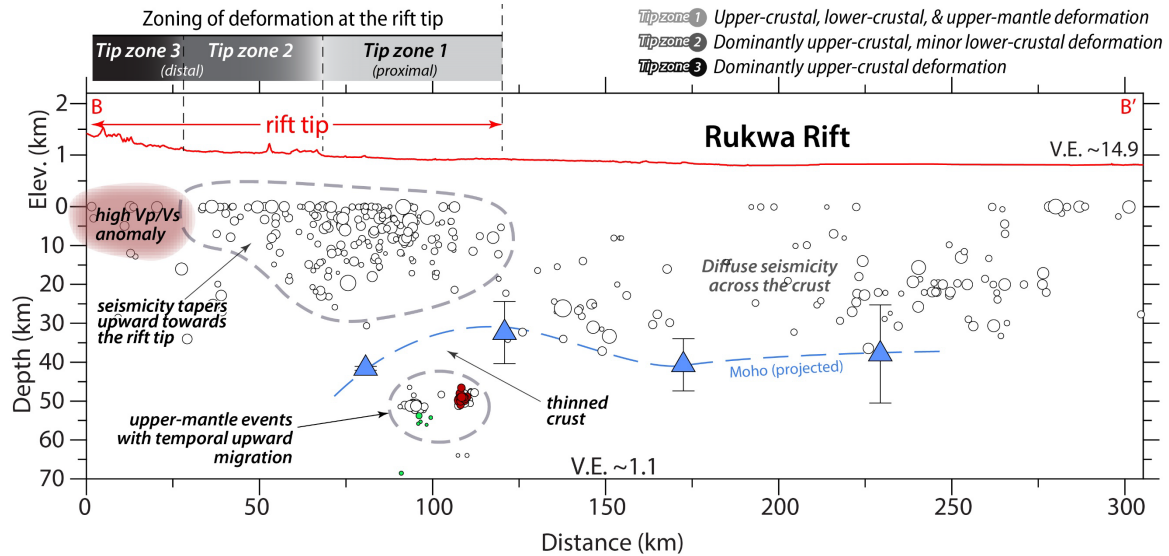
437
438

439 The spatial relationship between large earthquake clustering and the velocity distribution in the upper crust may provide insight
440 into how bulk rock alterations may influence seismicity and strain accommodation at the rift tips. The occurrence of geothermal
441 anomalies in the vicinity of the high Vp/Vs ratio anomalies suggest that ascending fluids may be advecting heat into the upper
442 crust. At both the Rukwa and Mweru-Wantipa Rift tips, we observe that the most prominent seismicity clustering occurs near
443 the margins of the high Vp/Vs ratio upper-crustal anomalies, and not within the anomalies (Figs. 3i,k,l). We infer that this
444 pattern indicates frictionally stable conditions promoting aseismic failure within the crustal blocks of high Vp/Vs ratio, and
445 frictionally unstable conditions promoting seismic failure in their surrounding crust. The brittle failure of brittle discontinuities
446 may be aseismic or seismic depending on confining stress, temperature, and compositional characteristics of the crust and the
447 fault rocks they host (e.g., Blanpied et al., 1991; Carpenter et al., 2011; Kolawole et al., 2019). Given the same loading
448 conditions around the rift tips, it is possible that significant fluid-rock alterations of the crust due to the migrating fluids within
449 the areas of highest Vp/Vs resulted in frictionally stable conditions within the zones of highest Vp/Vs ratios (D1 in Fig. 6a) as
450 opposed to their surrounding regions that are failing by seismogenic deformation (zone D2). Within the central regions of the
451 Rukwa Rift, the Vp/Vs anomaly A3 is collocated with an area of relatively less intra-rift fault occurrence (Fig. 5i) but is in the
452 hanging wall of the Ufipa border fault near a known geothermal anomaly (Jones, 2020). Since A3 is confined to <5 km depth
453 (Fig. 3k), it may also represent a compositionally altered and mechanically weakened section of the border fault and its hanging
454 wall block, similar to velocity anomalies observed near geothermal field of active rifts elsewhere (e.g., Hauksson and Unruh,
455 2007).

456

457 Although our results generally indicate active deformation at the propagating rift tips of the Rukwa and Mweru-Wantipa rifts,
458 the relatively greater abundance of data at the Rukwa Rift tip permit a characterization of how the controls on the deformation
459 may vary from the proximal rift tip zones to the distal tip zones. The depth distribution of seismicity and the detected
460 spatiotemporal seismicity clusters, the along-rift variation of crustal thickness, and relative location of high Vp/Vs anomaly
461 suggest that the proximal tip zones (tip zone 1) is dominated by upper-crustal, lower-crustal, and upper-mantle deformation
462 (Fig. 5). However, the crust appears to thicken towards the distal tip zones (tip zones 2 to 3) and the seismicity patterns appear
463 to become shallower and primarily focusing on the upper crust at tip zone 3 (Fig. 5). In general, we infer a through-going
464 crustal deformation in the proximal rift tip zones controlled by crustal thinning and infiltration of volatiles into the crust with
465 focused crustal bending strain (synclinal?), all of which transition into a dominantly upper-crustal deformation at the distal tip
466 zones where bending strain (anticlinal) and fluid-rock alterations control the brittle deformation. Published models for rift
467 linkage demonstrate that rift basins can propagate laterally and interact when in proximity (e.g., Allken et al., 2012; Corti,
468 2012; Molnar et al., 2019; Nelson et al., 1992; Zwaan et al., 2016; Zwaan and Schreurs, 2020; Neuharth et al., 2021; Kolawole
469 et al., 2021a). Models also show that laterally propagating rift tips may host stress concentration zones (van Wijk and
470 Blackman, 2005; Le Pourhiet et al., 2018). Our study presents evidence from a natural rift for the first time, revealing the
471 presence of crustal weakening at a laterally propagating continental rift tip, and in addition, shows how the weakening is likely
472 controlled by a combination of crustal bending strain and fluids (ascending volatiles and migrating hydrothermal fluids). We

473 propose a model for lateral rift propagation whereby progressive rift tip propagation is marked by the development of localized
474 weakened crust at the rift tip (Time T1, Fig. 6a) which subsequently gives way to a lengthened rift basin (Time T2, Fig. 6b).



499 **Figure 5.** Interpretation of longitudinal cross-sectional profile B-B' of the Rukwa Rift (same as in Fig. 2d and S24d) highlighting the spatial
500 relationships between the broad seismicity distribution, detected fluid-related clustered events (colored upper-mantle events), upper-crustal
501 low-velocity anomalies, moho depth distribution, and the zoning of active deformation at the rift-tip.

502
503

504

505

506

507

508

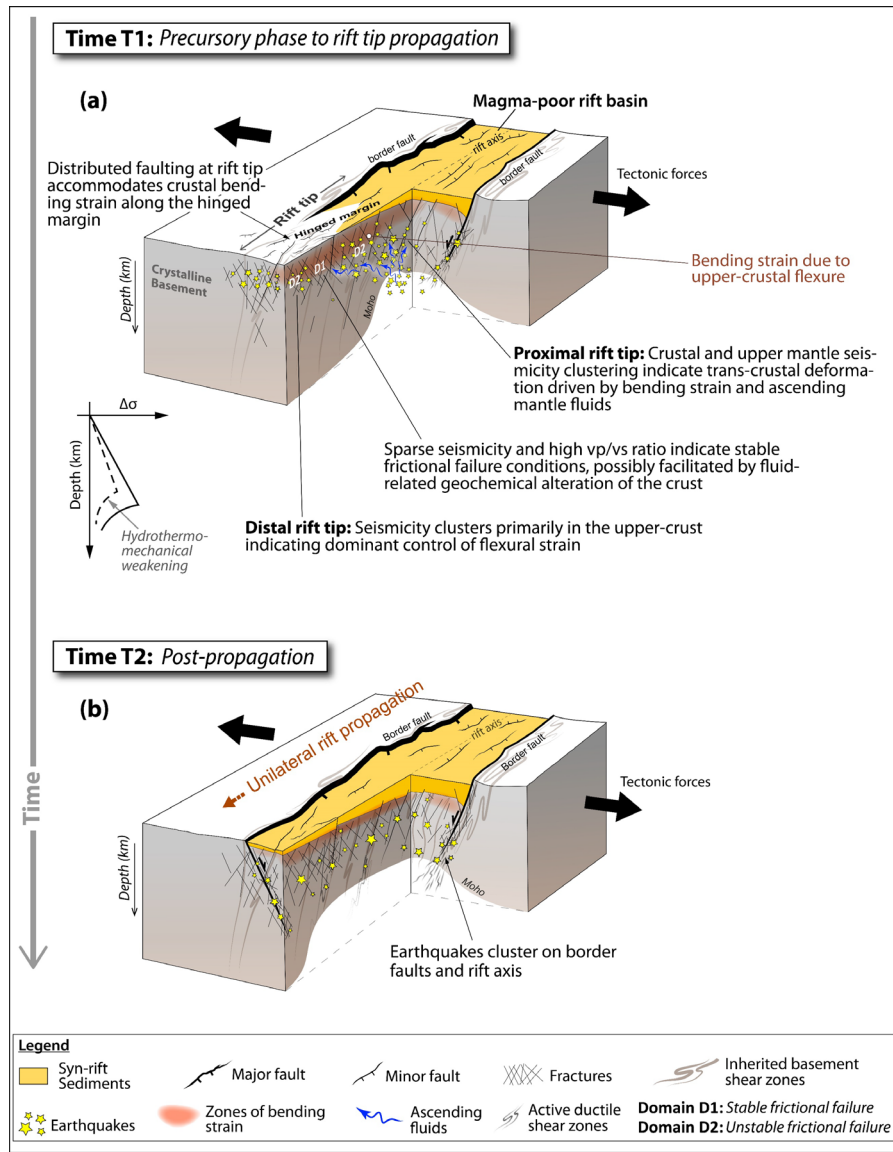


Figure 6. Cartoons showing the proposed model of crustal strain accommodation during the unilateral propagation phases of active continental rift tips, based on the results of our study. Note that the panel b of the cartoon is idealized to speculate a likelihood of decreased seismicity at a paleo-rift tip zone post propagation of the rift tip and does not include earthquakes occurrence due to other tectonic processes that may promote strain localization within the rift axis.

556 **Conclusions**

557 To understand how tectonic strain is accommodated along actively propagating magma-poor continental rifts, we constructed
558 three-dimensional velocity models of the crystalline crust beneath the Rukwa-Tanganyika Rift Zone where the Tanganyika
559 Rift is interacting with the Rukwa and Mweru-Wantipa rifts. The results show anomalously high V_p/V_s ratio anomalies at the
560 Rukwa and Mweru-Wantipa rift tips and their rift interaction zones with the Tanganyika Rift, representing, for the first time,
561 geophysical evidence demonstrating crustal softening of rift tips in a region of active unilateral rift propagation. We detect
562 distinct earthquake families within the deeper rift-tip seismicity clusters that exhibit linear upward migration patterns, and
563 temporal evolution patterns that suggest fluid migration and associated creep failure. We determine that brittle damage due to
564 bending strain and thermomechanical alteration of the crust by ascending fluids (mantle-sourced volatiles and hydrothermal
565 fluids) are accommodating the mechanical weakening at the rift tip to facilitate the propagation of the rift tip into unrifted crust
566 within the rift interaction zones. Furthermore, we observe a transition from collocated thinned crust and through-going crustal
567 and upper-mantle seismicity in the proximal tip zones, to dominantly upper-crustal seismicity in the distal tip zones, indicating
568 an along-axis variation in the controls on rift tip deformation. The results of this study provide new and compelling insights
569 into how continental rift tips propagate, link, and coalesce to form continuous axial rift floors — a necessary ingredient for
570 initiating large-scale continental break-up axes.

571

572 **Acknowledgments**

573 This project was supported by funds from the Columbia Climate School and the Vetlesen Foundation awarded to Folarin
574 Kolawole. We thank Finnigan Illsley-Kemp, Frank Zwaan, and anonymous reviewers for comments that helped to improve
575 the earlier and later versions of the manuscript. Some figures are plotted using GMT (Wessel et al., 2019).

576 **Author contributions**

577 F.K. and R.A. conceptualized the project. R.A. performed the modeling. F.K. and R.A. interpreted the results. F.K. wrote the
578 manuscript. R.A. revised the manuscript.

579 **Competing interests**

580 The authors declare no competing interests.

581 **Open Research**

582 Computer programs and files to reproduce our results are in Ajala and Kolawole (2023).

583 **References**

584

585 Aanyu, K. and Koehn, D., 2011. Influence of pre-existing fabrics on fault kinematics and rift geometry of interacting segments:
586 analogue models based on the Albertine Rift (Uganda), Western Branch-East African Rift System. *Journal of African*
587 *Earth Sciences*, 59(2-3), pp.168-184.

588 Acocella, Faccenna, Funiciello and Rossetti, 1999. Sand-box modelling of basement-controlled transfer zones in extensional
589 domains. *Terra Nova*, 11(4), pp.149-156.

590 Ajala, R., and Kolawole, F. (2023). Reproducibility material for crustal softening at propagating rift tips. Retrieved from
591 <https://doi.org/10.5281/zenodo.8302196>

592 Ajala, R., Kolawole, F. and Menke, W., 2024. Blind magmatism abets nonvolcanic continental rifting. *Communications*
593 *Earth & Environment*, 5(1), p.80.

594 Ajala, R. and Persaud, P. (2021). Effect of Merging Multiscale Models on Seismic Wavefield Predictions Near the Southern
595 San Andreas Fault. *Journal of Geophysical Research: Solid Earth*, 126, 1-23.

596 Allam, A. A., Ben-Zion, Y., Kurzon, I., and Vernon, F., 2014. Seismic velocity structure in the Hot Springs and Trifurcation
597 areas of the San Jacinto fault zone, California, from double-difference tomography. *Geophysical Journal*
598 *International*, 198, 978-999.

599 Allken, V., Huisman, R.S. and Thieulot, C., 2012. Factors controlling the mode of rift interaction in brittle-ductile coupled
600 systems: A 3D numerical study. *Geochemistry, Geophysics, Geosystems*, 13(5).

601 Blanpied, M.L., Lockner, D.A. and Byerlee, J.D., 1991. Fault stability inferred from granite sliding experiments at
602 hydrothermal conditions. *Geophysical Research Letters*, 18(4), pp.609-612.

603 Brune, S., Kolawole, F., Olive, J.A., Stamps, D.S., Buck, W.R., Buiter, S.J., Furman, T. and Shillington, D.J., 2023.
604 Geodynamics of continental rift initiation and evolution. *Nature Reviews Earth & Environment*, 4(4), pp.235-253.

605 Carpenter, B.M., Marone, C. and Saffer, D.M., 2011. Weakness of the San Andreas Fault revealed by samples from the active
606 fault zone. *Nature Geoscience*, 4(4), pp.251-254.

607 Celli, N. L., Lebedev, S., Schaeffer, A. J., and Gaina, C. (2020). African cratonic lithosphere carved by mantle plumes. *Nature*
608 *Communications*, 11(92), 1-10.

609 Chatterjee, S.N., Pitt, A.M. and Iyer, H.M., 1985. Vp/Vs ratios in the Yellowstone national park region, Wyoming. *Journal of*
610 *Volcanology and Geothermal Research*, 26(3-4), pp.213-230.

611 Chen, Y.L., Ni, J., Shao, W. and Azzam, R., 2012. Experimental study on the influence of temperature on the mechanical
612 properties of granite under uni-axial compression and fatigue loading. *International Journal of Rock Mechanics and*
613 *Mining Sciences*, 56, pp.62-66.

614 Cormier, V. F. and Spudich. (1984). Amplification of ground motion and waveform complexity in fault zones: examples from
615 the San Andreas and Calaveras Faults. *Geophys. J. R. astr. Soc.*, 79, 135–152.

616 Corti, G., 2004. Centrifuge modelling of the influence of crustal fabrics on the development of transfer zones: insights into the
617 mechanics of continental rifting architecture. *Tectonophysics*, 384(1-4), pp.191-208.

618 Craig, T. J., Jackson, J. A., Priestley, K., and McKenzie, D. (2011). Earthquake distribution patterns in Africa: Their
619 relationship to variations in lithospheric and geological structure, and their rheological implications. *Geophysical*
620 *Journal International*, 185(1), 403–434. <https://doi.org/10.1111/j.1365-246X.2011.04950.x>

621 Daly, M. C. (1988). Crustal Shear Zones in Central Africa: a Kinematic Approach to Proterozoic Tectonics. *Episodes* 11 (1),
622 5–11. doi:10.18814/epiiugs/1988/v11i1/003

623 Delvaux, D., 1989. The Karoo to recent rifting in the western branch of the East-African Rift System: a bibliographical
624 synthesis. In: *Mus. Roy. Afr. Centr., Tervuren (Belg.)*, Dept. Geol. Min., Rapp. Ann, 1990, 1991, pp. 63–83.

625 Delvaux, D., and Barth, A. (2010). African stress pattern from formal inversion of focal mechanism data. *Tectonophysics*,
626 482(1–4), 105–128. <https://doi.org/10.1016/j.tecto.2009.05.009>.

627 Delvaux, D., Kervyn, F., Macheyeki, A. S., and Temu, E. B. (2012). Geodynamic Significance of the TRM Segment in the
628 East African Rift (W-Tanzania): Active Tectonics and Paleostress in the Ufipa Plateau and Rukwa basin. *J. Struct.*
629 *Geology*. 37, 161–180.

630 Fang, H., Yao, H., Zhang, H., Thurber, C., Ben-Zion, Y. and van der Hilst, R.D., 2019. V p/V s tomography in the southern
631 California plate boundary region using body and surface wave travelttime data. *Geophysical Journal International*,
632 216(1), pp.609-620.

633 Foster, A. N., and Jackson, J. A. (1998). Source parameters of large African earthquakes: Implications for crustal rheology
634 and regional kinematics. *Geophysical Journal International*, 134(2), 422–448. [https://doi.org/10.1046/j.1365-](https://doi.org/10.1046/j.1365-246x.1998.00568.x)
635 246x.1998.00568.x

636 Gaherty, J.B., Zheng, W., Shillington, D.J., Pritchard, M.E., Henderson, S.T., Chindandali, P.R.N., Mdala, H., Shuler, A.,
637 Lindsey, N., Oliva, S.J. and Nooner, S., 2019. Faulting processes during early-stage rifting: Seismic and geodetic
638 analysis of the 2009–2010 Northern Malawi earthquake sequence. *Geophysical Journal International*, 217(3),
639 pp.1767-1782.

640 Ganbat, A., Tsujimori, T., Boniface, N., Pastor-Galán, D., Aoki, S. and Aoki, K., 2021. Crustal evolution of the
641 Paleoproterozoic Ubendian Belt (SW Tanzania) western margin: a Central African Shield amalgamation tale.
642 *Gondwana Research*, 91, pp.286-306.

643 Goebel, T. H. W., Rosson, Z., Brodsky, E. E., & Walter, J. I. (2019). Aftershock deficiency of induced earthquake sequences
644 during rapid mitigation efforts in Oklahoma. *Earth and Planetary Science Letters*, 522, 135-143.

645 Goetze, C. and Evans, B., 1979. Stress and temperature in the bending lithosphere as constrained by experimental rock
646 mechanics. *Geophysical Journal International*, 59(3), pp.463-478.

647 Hanson, R.E., 2003. Proterozoic geochronology and tectonic evolution of southern Africa. Geological Society, London,
648 Special Publications, 206(1), pp.427-463.

649 Hauksson, E. and Unruh, J. (2007). Regional tectonics of the Coso geothermal area along the intracontinental plate boundary
650 in central eastern California: three-dimensional Vp and Vp/Vs models, spatio-temporal seismicity patterns, and
651 seismogenic deformation, *Journal of Geophysical Research*, 112(B6), 1-24.

652 Heilman, E., Kolawole, F., Atekwana, E. A., and Mayle, M. (2019). Controls of Basement Fabric on the Linkage of Rift
653 Segments. *Tectonics* 38 (4), 1337–1366. doi:10.1029/2018tc005362.

654 Hodgson, I., Illsley-Kemp, F., Gallacher, R., Keir, D., Ebinger, C. J., and Mtelega, K. (2017). Crustal Structure at a Young
655 Continental Rift: A Receiver Function Study from the Tanganyika Rift. *Tectonics*, 36, 1-17.

656 Hole, J. A. (1992). Nonlinear high-resolution three-dimensional seismic travel time tomography. *Journal of Geophysical*
657 *Research: Solid Earth*, 97(B5), 6553-6562. <http://dx.doi.org/10.1029/92JB00235>

658 Jones, D. J. R. (2020). A summary of the East Africa Rift Temperature and Heat flow Model (EARTH). British Geological
659 Survey Open Report, OR/20/006. 24pp.

660 Kolawole, F., Firkins, M.C., Al Wahaibi, T.S., Atekwana, E.A. and Soreghan, M.J., 2021a. Rift interaction zones and the
661 stages of rift linkage in active segmented continental rift systems. *Basin Research*, 33(6), pp.2984-3020.

662 Kolawole, F., Johnston, C.S., Morgan, C.B., Chang, J.C., Marfurt, K.J., Lockner, D.A., Reches, Z. and Carpenter, B.M., 2019.
663 The susceptibility of Oklahoma’s basement to seismic reactivation. *Nature Geoscience*, 12(10), pp.839-844.

664 Kolawole, F., Phillips, T.B., Atekwana, E.A. and Jackson, C.A.L., 2021b. Structural inheritance controls strain distribution
665 during early continental rifting, rukwa rift. *Frontiers in Earth Science*, 9, p.707869.

666 Kolawole, F., Vick, T., Atekwana, E.A., Laó-Dávila, D.A., Costa, A.G., and Carpenter, B.M. (2022). Strain Localization and
667 Migration During the Pulsed Lateral Propagation of the Shire Rift Zone, East Africa. *Tectonophysics*, 839, 229499.
668 Doi: 10.1016/j.tecto.2022.229499.

669 Kolawole, F., Xue, L. and Dulanya, Z., 2023. Rapid Versus Delayed Linkage and Coalescence of Propagating Rift Tips.
670 *Authorea Preprints*, 10.22541/essoar.168167202.29986035/v1.

671 Kranz, R. L. (1979). Crack-crack and crack-pore interactions in stressed granite. *International Journal of Rock Mechanics and*
672 *Mining Sciences and Geomechanics Abstracts*, 16(1), 37–47.

673 Lavayssière, A., Drooff, C., Ebinger, C. J., Gallacher, R., Illsley-Kemp, F., Oliva, S. J., and Keir, D. (2019). Depth Extent and
674 Kinematics of Faulting in the Southern Tanganyika Rift, Africa. *Tectonics*, 38, 842-862.

675 Lemna, O. S., Stephenson, R., and Cornwell, D. G. (2019). The Role of Pre-existing Precambrian Structures in the
676 Development of Rukwa Rift Basin, Southwest Tanzania. *J. Afr. Earth Sci.* 150, 607–625.
677 doi:10.1016/j.jafrearsci.2018.09.015.

678 Le Pourhiet, L., Chamot-Rooke, N., Delescluse, M., May, D.A., Watremez, L. and Pubellier, M., 2018. Continental break-up
679 of the South China Sea stalled by far-field compression. *Nature Geoscience*, 11(8), pp.605-609.

680 Molnar, N.E., Cruden, A.R. and Betts, P.G., 2019. Interactions between propagating rifts and linear weaknesses in the lower
681 crust. *Geosphere*, 15(5), pp.1617-1640.

- 682 Morley, C. K., Cunningham, S. M., Harper, R. M., and Wescott, W. A. (1992). Geology and Geophysics of the Rukwa Rift,
683 East Africa. *Tectonics* 11 (1), 69–81. doi:10.1029/91tc02102.
- 684 Morley, C. K., Wescott, W. A., Harper, R. M., and Cunningham, S. M. (1999). Geology and Geophysics of the Rukwa Rift.
685 *Geoscience of Rift Systems-Evolution of East Africa*. AAPG Stud. Geology. 44, 91–110.
- 686 Muirhead, J. D., Wright, L. J., and Scholz, C. A. (2019). Rift evolution in regions of low magma input in East Africa. *Earth
687 and Planetary Science Letters*, 506, 332–346.
- 688 Mulaya, E., Gluyas, J., McCaffrey, K., Phillips, T. and Ballentine, C. (2022). Structural geometry and evolution of the Rukwa
689 Rift Basin, Tanzania: Implications for helium potential. *Basin Research* 34, 938-960.
- 690 Nakajima, J., Matsuzawa, T., Hasegawa, A. and Zhao, D., 2001. Three-dimensional structure of V_p, V_s, and V_p/V_s beneath
691 northeastern Japan: Implications for arc magmatism and fluids. *Journal of Geophysical Research: Solid Earth*,
692 106(B10), pp.21843-21857.
- 693 Nelson, R.A., Patton, T.L. and Morley, C.K., 1992. Rift-segment interaction and its relation to hydrocarbon exploration in
694 continental rift systems. *AAPG bulletin*, 76(8), pp.1153-1169.
- 695 Neuharth, D., Brune, S., Glerum, A., Heine, C. and Welford, J.K., 2021. Formation of continental microplates through rift
696 linkage: Numerical modeling and its application to the Flemish Cap and Sao Paulo Plateau. *Geochemistry,
697 Geophysics, Geosystems*, 22(4), p.e2020GC009615.
- 698 Njinju, E.A., Atekwana, E.A., Stamps, D.S., Abdelsalam, M.G., Atekwana, E.A., Mickus, K.L., Fishwick, S., Kolawole, F.,
699 Rajaonarison, T.A. and Nyalugwe, V.N., 2019. Lithospheric structure of the Malawi Rift: Implications for magma-
700 poor rifting processes. *Tectonics*, 38(11), pp.3835-3853.
- 701 Nunn, J.A., 1985. State of stress in the northern Gulf Coast. *Geology*, 13(6), pp.429-432.
- 702 Olson, J.E., 2004. Predicting fracture swarms—The influence of subcritical crack growth and the crack-tip process zone on
703 joint spacing in rock. *Geological Society, London, Special Publications*, 231(1), pp.73-88.
- 704 Pérez-Gussinyé, M., Collier, J.S., Armitage, J.J., Hopper, J.R., Sun, Z. and Ranero, C.R., 2023. Towards a process-based
705 understanding of rifted continental margins. *Nature Reviews Earth & Environment*, 4(3), pp.166-184.
- 706 Raggiunti, M., Keir, D., Pagli, C., & Lavayssière, A. (2023). Evidence of Fluid Induced Earthquake Swarms From High
707 Resolution Earthquake Relocation in the Main Ethiopian Rift. *Geochemistry, Geophysics, Geosystems*, 24, 1-16.
- 708 Reasenber, P. (1985). Second-Order Moment of Central California Seismicity, 1969-1982. *Journal of Geophysical Research*,
709 90(87), 5479-5495.
- 710 Roberts, E. M., Stevens, N. J., O'Connor, P. M., Dirks, P. H. G. M., Gottfried, M. D., Clyde, W. C., Armstrong, R. A., Kemp,
711 A. I. S., and Hemming, S. (2012). Initiation of the western branch of the East African Rift coeval with the eastern
712 branch. *Nature Geoscience*, 5(4), 289–294. <https://doi.org/10.1038/ngeo1432>.
- 713 Roland, M., & McGuire, J. J. (2009). Earthquake swarms on transform faults. *Geophysical Journal International*, 178, 1677-
714 1690.
- 715 Saeidi, H., Hansen, S.E., Nyblade, A.A. and Haag, R., 2024. Mantle structure beneath the Damara Belt in south-central Africa
716 imaged using adaptively parameterized P-wave tomography. *Journal of Geophysical Research: Solid Earth*, 129(3),
717 p.e2023JB027965.
- 718 Shaban, S., Scholz, C.A., Kolawole, F. (2023). The Deep Basin and Underlying Basement Structure of the Tanganyika Rift.
719 *Tectonics*, 42, e2022TC007726.
- 720 Stamps, D. S., Calais, E., Saria, E., Hartnady, C., Nocquet, J. M., Ebinger, C. J., and Fernandes, R. M. (2008). A kinematic
721 model for the East African Rift. *Geophysical Research Letters*, 35(5).
- 722 Stein, S., Sleep, N.H., Geller, R.J., Wang, S.C. and Kroeger, G.C., 1979. Earthquakes along the passive margin of eastern
723 Canada. *Geophysical Research Letters*, 6(7), pp.537-540.
- 724 Stevens, V.L., Sloan, R.A., Chindandali, P.R., Wedmore, L.N., Salomon, G.W., Muir, R.A., 2021. The entire crust can be
725 seismogenic: evidence from Southern Malawi. *Tectonics* 40 (6). <https://doi.org/10.1029/2020TC006654>
726 e2020TC006654.
- 727 Tiercelin, J.J., Pflumio, C., Castrec, M., Boulégué, J., Gente, P., Rolet, J., Coussement, C., Stetter, K.O., Huber, R., Buku, S.
728 and Mifundu, W., 1993. Hydrothermal vents in Lake Tanganyika, East African, Rift system. *Geology*, 21(6), pp.499-
729 502.

730 Van Herwaarden, D., Thrastarson, S., Halpa, V., Afanasiev, M., Trampert, J., and Fichtner, A. (2022). Full-Waveform
731 Tomography of the African Plate Using Dynamic Mini-Batches. *Journal of Geophysical Research: Solid Earth*, 126,
732 1-22.

733 Van Wijk, J.K., Blackman, D.K., 2005. Dynamics of continental rift propagation: the endmember modes. *Earth Planet. Sci.*
734 *Lett.* 229 (3-4), 247-258.

735 Veatch, A. C. (1935). Evolution of the Congo Basin. *GSA Memoir* 3.

736 Versfelt, J., and Rosendahl, B. (1989). Relationship between pre-rift structure and rift architecture in Lakes Tanganyika and
737 Malawi, East Africa. *Nature*, 337, 354-357.

738 Vidale, J. E. (1990). Finite-difference calculation of traveltimes in three dimensions. *Geophysics*, 55(5), 521-526.

739 Wessel, P., Luis, J. F., Uieda, L., Scharroo, R., Wobbe, F., Smith, W. H. F., and Tian, D. (2019). The generic mapping tools
740 version 6. *Geochemistry, Geophysics, Geosystems*, 20, 1-20. <https://doi.org/10.1029/2019gc008515>

741 Yang, Z., and Chen, W. P. (2010). Earthquakes along the East African Rift System: A multiscale, system-wide perspective.
742 *Journal of Geophysical Research*, 115, B12309. <https://doi.org/10.1029/2009JB006779>

743 Zaliapin, I., & Ben-Zion, Y. (2013). Earthquake clusters in southern California I: Identification and stability. *Journal of*
744 *Geophysical Research: Solid Earth*, 118, 2847-2864.

745 Zaliapin, I., Gabrielov, A., Keilis-Borok, V., & Wong, H. (2008). Clustering Analysis of Seismicity and Aftershock
746 Identification. *Physical Review Letters*, 101, 1-4.

747 Zhang, Q., & Shearer, P. (2016). A new method to identify earthquake swarms applied to seismicity near the San Jacinto Fault,
748 California. *Geophysical Journal International*, 205, 995-1005.

749 Zheng, W., Oliva, S.J., Ebinger, C. and Pritchard, M.E., 2020. Aseismic deformation during the 2014 M w 5.2 Karonga
750 earthquake, Malawi, from satellite interferometry and earthquake source mechanisms. *Geophysical Research Letters*,
751 47(22), p.e2020GL090930.

752 Zwaan, F., and Schreurs, G. (2020). Rift segment interaction in orthogonal and rotational extension experiments: Implications
753 for the large-scale development of rift systems. *Journal of Structural Geology*, 140, 104119.
754 <https://doi.org/10.1016/j.jsg.2020.104119>

755 Zwaan, F., Schreurs, G., Naliboff, J., and Buitter, S. J. (2016). Insights into the effects of oblique extension on continental rift
756 interaction from 3D analogue and numerical models. *Tectonophysics*, 693, 239-260.
757 <https://doi.org/10.1016/j.tecto.2016.02.036>